Chinese Chemical Letters 35 (2024) 109990

Contents lists available at ScienceDirect

Chinese Chemical Letters

journal homepage: www.elsevier.com/locate/cclet

Encapsulating Si particles in multiple carbon shells with pore-rich for constructing free-standing anodes of lithium storage

Xianping Du[a], Ying Huang[a,*], Chen Chen[b], Zhenhe Feng[c], Meng Zong[a,*]

[a] MOE Key Laboratory of Material Physics and Chemistry under Extraordinary Conditions, School of Chemistry and Chemical Engineering, Northwestern Polytechnical University, Xi'an 710072, China
[b] School of Electrical Engineering, Xi'an University of Technology, Xi'an 710048, China
[c] Shanghai Institute of Space Power-sources, Shanghai 200245, China

ARTICLE INFO

Article history:
Received 1 April 2024
Revised 20 April 2024
Accepted 9 May 2024
Available online 10 May 2024

Keywords:
Si particles, rGO nanosheets
Core@multi-shell
Free-standing anodes
lithium-ion batteries

ABSTRACT

Silicon based (Si-based) materials are considered to be the most promising anode materials for lithium-ion batteries (LIBs) due to their high specific capacity. However, the issues of poor electrical conductivity and volume expansion during cycling have not been effectively addressed. The optimum remedy is to select specific materials to establish an exceptional conductive and volume buffer structure to assist the Si materials to develop its excellent lithium storage properties. Here, Si particles were encapsulated into porous carbon fibers containing ultrafine Co particles (CP) to obtained Si-x@CP-y film. Among them, the addition of Si particles and the void structure was precisely regulated to achieve a superior electrode with a high specific capacity. Subsequently, the two-dimensional conductive material reduced graphene oxide (rGO) nanosheets were further incorporated to obtain Si-2@CP-2@rGO films with core@multi-shell structure. The final electrode was equipped with one-, two-, and three-dimensional electronic pathways to allow rapid electron transport, and featured with multi-layer buffer structure and reserved pores that could effectively mitigate volume changes. As expected, the free-standing Si-2@CP-2@rGO electrode delivered a high specific capacity of 1221.2 mAh/g after 100 cycles at 0.1 A/g in a half cell, and the assembled full cell showed 249.0 mAh/g after 200 cycles at 0.2 A/g, which fulfilled the lightweight requirement for new energy storage devices.

The rapid development of the energy storage industry puts higher requirements on lithium-ion batteries (LIBs) [1]. Commercially available graphite has a low theoretical capacity and cannot meet the requirements of future energy storage devices [2–4]. Silicon-based (Si-based) materials are regarded as a prospective anode material with high specific capacity and low charge/discharge plateaus [5–7]. However, the poor electrical conductivity and significant volume changes during cycling has always been a bottleneck for Si-based materials [8–10].

The most effective response to the issue of large volume changes during cycling is to create a robust buffer structure. The structures included sandwiches [11], core@shell [12], core@multi-shell [13], *etc*., which all proved to be effective in mitigating electrode volume changes. Among them, core@multi-shell structure offers a significant advantage in mitigating volume expansion. The robust multiple shells ensure that the electrodes maintain their integrity during cycling. In addition, the deliberate design of the void structure is also a specific measure to reduce the volume change. The voids can absorb the internal stress to maintain the integrity of the electrode structure [14].

In light of the inferior conductivity of Si-based materials, it is typically enhanced by incorporating selected materials with good electrical conductivity. Carbon fibers (CFs) possess significant electrical conductivity and are equipped with one-dimensional conductive pathways. Reduced graphene oxide (rGO) is extensively utilized in energy storage as a two-dimensional conductive material due to its low density, large specific surface area, and high charge carrier mobility. rGO can also enhance the physical connection points between fibers and reduce the interfacial resistance to improve the final electrochemical performance. In addition, ultrafine Co nanoparticles with a high specific surface area can provide uniform lithium nucleation sites. This can help reduce the local current density, promote even lithium deposition, and prevent the growth of lithium dendrites [15]. Co particles can also catalyze the decomposition of SiO_2 and inactive Li_2O during cycling of Si electrodes [16]. It has also been demonstrated that Co doping with

* Corresponding authors.
E-mail addresses: yingh@nwpu.edu.cn (Y. Huang), zongmeng@nwpu.edu.cn (M. Zong).

https://doi.org/10.1016/j.cclet.2024.109990
1001-8417/

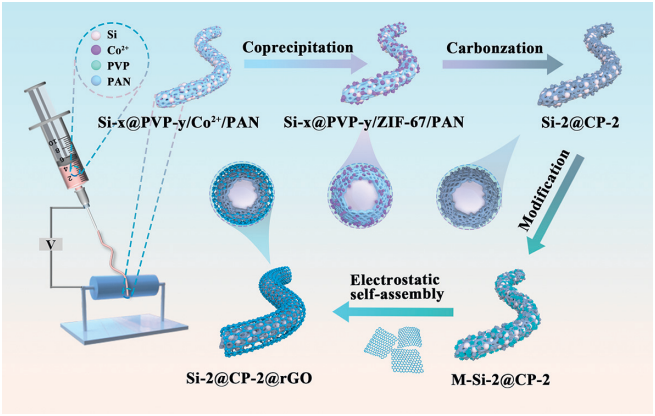

Fig. 1. Illustration of the synthesis of Si-2@CP-2@rGO films.

Si-based electrodes helps in achieving high initial Coulombic efficiency (ICE) [17]. The presence of Co particles will also enhance the graphitization of carbon materials [18].

Herein, Si particles were well encapsulated inside porous CFs containing ultrafine Co particle (Si-x@CP-y), where the addition of Si particles and the porous structure were precisely regulated to achieve superb electrochemical properties. Subsequently, rGO nanosheets were wrapped on the Si-2@CP-2 surface through electrostatic self-assembly. The ultimately available core@multi-shell Si-2@CP-2@rGO films exhibited some advantages. (1) The CFs and rGO cooperated to establish interpenetrating conductive networks with one-, two-, and three-dimensional electronic pathways through deliberate structural modulation. (2) The final Si-2@CP-2@rGO electrode was equipped with robust buffer layers and a designed void structure, which could absorb the stress caused by the volume change of Si particles. (3) In comparison with the traditional powder electrode, the free-standing Si-2@CP-2@rGO film eliminated the introduction of inactive substances and met the demand for lightweighting in new energy storage devices. Additionally, it presented more possibilities for developing flexible electronics.

Fig. 1 shows a synthetic schematic of Si-2@CP-2@rGO film. Monodisperse SiO_2 and porous Si particles were presented in Figs. S1a and b (Supporting information), Fig. 2a and Fig. S2a (Supporting information), respectively. The diffraction rings in its edge region corresponded to the (111), (220), and (311) crystal planes (PDF#27–1402) in selected area electron diffraction (SAED) (Fig. S2b in Supporting information) [19]. EDS mapping and high-resolution transmission electron microscopy (HRTEM) images further supported the synthesis of Si particles (Figs. S2c-g in Supporting information). The Si-x@CP-y series films were presented in Fig. 2b and Figs. S3a-e (Supporting information). Si-2@CP-2 fibers exhibited a uniform distribution of Si particles inside the fibers. Both excessive and insufficient addition of Si particles were detrimental to their electrochemical properties. Further, the amount of polyvinyl pyrrolidone (PVP) was varied to produce Si-2@CP-1 and Si-2@CP-3 films. It could be observed that no voids existed on Si-2@CP-1 fibers, while the Si-2@CP-3 fibers appeared to fracture. This situation is not conducive to the stabilization of the electrode structure during cycling. Transmission electron microscopy (TEM) images confirmed the presence of Si and Co particles (Fig. 2c). The Si (111), Co (111), and Co (200) diffraction rings were visualized in the SAED image (Fig. 2d). HRTEM and EDS mapping results agreed with the above view (Fig. 2e and Fig. S4a-e in Supporting information). Subsequently, rGO nanosheets were tightly wrapped around the Si-2@CP-2 surface (Figs. 2f and g). HADDF and EDS mapping analysis further validated that the final Si-2@CP-2@rGO films were obtained (Figs. 2h and i). The content of rGO was also regulated in Fig. S5 (Supporting information).

X-ray diffraction (XRD) analysis was conducted to examine the crystal structure of Si particles and Si-x@CP-y film (PDF#27–1402) (Fig. 2j and Fig. S6 in Supporting information) [19]. Among them, it was observed that the peaks of Si particles were barely detectable on the Si-1@CP-2 film. In contrast, there were only peaks of Si particles on the Si-4@CP-2 film, due to the larger addition of Si particles. The related peaks of Co metal also appeared, which could increase the graphitization degree of carbon fiber (Fig. S7 in Supporting information) [20]. In addition, compared to the Si-2@CP-2 film, the intensity of the broad peak between 20° and 30° increased for Si-2@CP-2@rGO films, indicating the presence of rGO nanosheets.

Fig. S8a (Supporting information) presented the X-ray photoelectron spectroscope (XPS) full spectra of the Si-2@CP-2@rGO samples. C 1s, N 1s, and O 1s spectra revealed the different bonding states of C, N, and O atoms (Figs. S8b-d in Supporting information) [21,22]. Fig. S8e (Supporting information) showed the relevant chemical bonds of Si species in the deconvoluted Si spectrum, in consistent with the literature reports [23,24]. In addition, the peaks at 778.7 and 793.8 eV were assigned to Co $2p_{3/2}$ and Co $2p_{1/2}$ of ultrafine metallic Co, while the peaks at 781.2 and 796.3 eV were attributed to Co $2p_{3/2}$ and Co $2p_{1/2}$ of Co^{2+}, and the remaining peaks were associated with satellite peaks (Fig. S8f in Supporting information) [25]. The Si-2@CP-2@rGO samples contained 32.21 wt% Si particles, 52.47 wt% porous carbon fibers, 2.08 wt% rGO nanosheets, and 6.23 wt% metal Co (Figs. S9a and b, Table S1 in Supporting information).

The pore size distribution of the samples was determined using the N_2 adsorption/desorption method (Figs. 2k-l, Figs. S10a and b in Supporting information). All the samples exhibited typical type IV isothermal curves and H3-Type hysteresis loops, indicating a mesoporous structure in the samples. This structure could enhance the adsorption of electrolyte ions and improve the electrochemical performance [26,27]. The specific surface areas of the Si particles, Si-1@CP-2, Si-2@CP-2, Si-3@CP-2, Si-4@CP-2, Si-2@CP-1, and Si-2@CP-3 and Si-2@CP-2@rGO samples were 93.01, 86.25, 83.92, 73.94, 58.45, 29.26, 110.49, and 125.89 m^2/g, respectively. This enhancement facilitated the rapid penetration of the electrolyte and also provided additional buffer space for accommodating the volume change of electrodes during cycling.

The electrochemical behaviors of the electrodes were investigated through cyclic voltammetry (CV) tests in the range of 0.01-3.0 V at a scan rate of 0.1 mV/s. The weak peak at 1.0 V in the initial cycle of the Si electrode was assigned to the irreversible generation of the solid electrolyte film (SEI) (Fig. S11a in Supporting information). The peak at 0.19 V in subsequent cycles was attributed to the alloying reaction of Si with lithium ions, while peaks at 0.31 and 0.5 V were identified as peaks of the de-alloying reaction. The voltage plateaus observed in the first four cycles were consistent with the alloying and de-alloying peaks demonstrated in the CV curves (Fig. S11b in Supporting information). The CV and charge/discharge behaviors of Si-x@CP-y electrodes were investigated by evaluating the representative Si-2@CP-2 electrodes, which only exhibited the characteristic peaks of the Si substance (Figs. S12a and b in Supporting information). Similarly, the Si-2@CP-2@rGO electrode also exhibited peaks corresponding to Si species at 0.19, 0.31, and 0.5 V (Figs. 3a and b), indicating that the presence of CP-2 and rGO did not change the electrochemical characteristics of the Si material.

The Si, Si-2@CP-2, and Si-2@CP-2@rGO electrodes exhibited charge/discharge specific capacities of 969.7/1590.3, 1413.1/1980.1, and 1617.0/1899.5 mAh/g in the first cycle, respectively, with ICE of 60.1%, 71.4%, and 85.1% (Fig. S13 in Supporting information). The CP and rGO nanosheets prevented the exposure of Si particles to the electrolyte, and also maintained the stability of the electrode

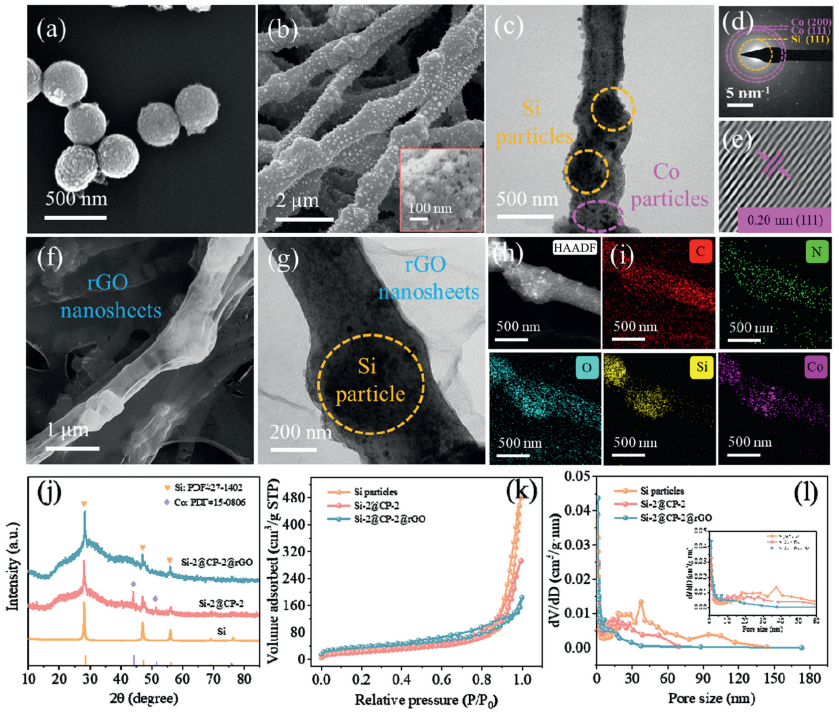

Fig. 2. (a) SEM analysis of Si particles. (b) SEM, (c) TEM, (d) SAED and (e) HRTEM images of the Si-2@CP-2 film. (f) SEM, (g) TEM, (h) HAADF and (i) EDS mapping of Si-2@CP-2@rGO films. (j) XRD pattern. (k) N_2 adsorption-desorption isotherm and (l) the pore size distribution.

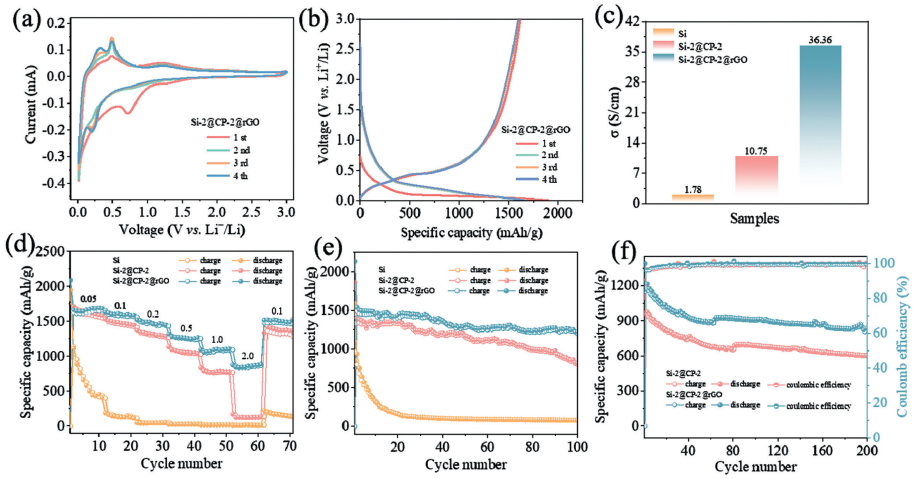

Fig. 3. (a) CV and (b) the initial charge/discharge curves of the Si-2@CP-2@rGO electrodes. (c) Comparison of the conductivity, (d) rate performance, cycling performance at (e) 0.1 A/g and (f) 1.0 A/g of the obtained electrodes.

structure. The introduction of CP and rGO would enhance the conductivity of the final electrode, thereby promoting the ICE. It has also been demonstrated that Co doping with Si-based electrodes helps in obtaining high ICE [17] .

The physical property measurement system (PPMS) was employed to determine the conductivity of the electrodes using the van der Pauw method. Fig. S14 (Supporting information) indicated that the resistance R_{nv} of the Si, Si-2@CP-2, and Si-2@CP-2@rGO electrodes were 1766.33, 272.96 and 78.09 Ω, respectively. The thicknesses of the Si, Si-2@CP-2, and Si-2@CP-2@rGO electrodes were 70, 75, and 78 μm, corresponding to conductivities of 1.78, 10.75, and 36.36 S/m, respectively (Fig. 3c). The above results further confirmed that the CP and rGO nanosheets significantly improved the conductivity of the final electrodes.

The rate performance and cycling performance are critical indicators for evaluating the practicality of electrodes. As shown in Fig. 3d and Fig. S15a (Supporting information), Si electrodes exhibited poor rate performance, which was closely linked to their low conductivity and the significant volume change during cycling. The rate performance of the Si-2@CP-2 electrode outperformed from Si-x@CP-y series electrodes. This superiority was attributed to the controlled the addition of Si particles and the design of the void structure. The Si-2@CP-2@rGO electrodes exhibited specific capacities of 1689.6, 1587.7, 1457.9, 1252.9, 1099.9, and 879.4 mAh/g at 0.05–2.0 A/g, respectively. When the current was adjusted back to 0.01 A/g, the specific capacity still reached 1486.1 mAh/g, with a recovery rate of 93.6%. As could be seen from Fig. 3e and Fig. S15b (Supporting information), the Si-2@CP-2@rGO electrodes also possessed an optimal reversible specific capacity of 1221.2 mAh/g after 100 cycles (0.1 A/g). The long-term cycling performance of the Si-2@CP-2 and Si-2@CP-2@rGO electrodes was further evaluated and maintained reversible specific capacities of 600.3 and 833.3 mAh/g,

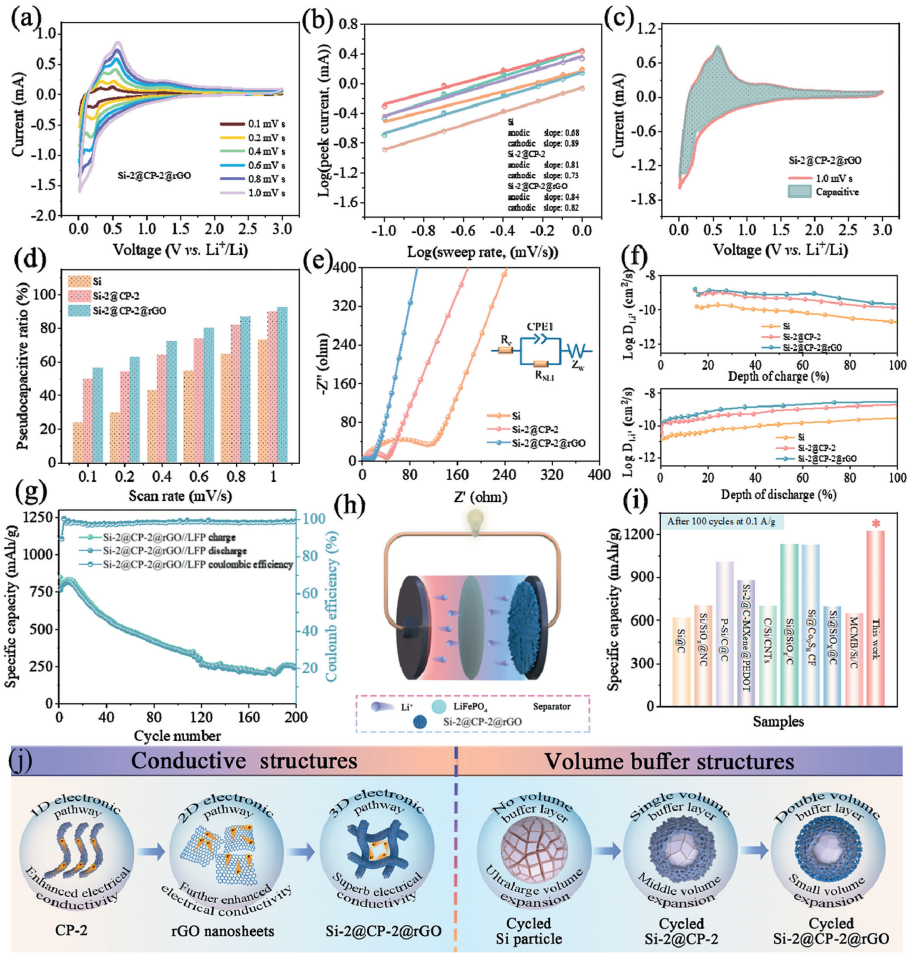

Fig. 4. (a) CV curves, (b) *b*-value of fitting results, (c) percentage of the capacitance of the Si-2@CP-2@rGO electrode. (d) The capacitance contributions, (e) EIS and (f) logD_{Li^+} of the obtained electrodes. (g) Cycling performance and (h) cycling mechanism of the Si-2@CP-2@rGO//LFP. (i) Comparison of this work with other Si-based electrodes [28-35]. (j) Schematic of structural characteristics of Si-2@CP-2@rGO electrodes.

respectively, after 200 cycles (1.0 A/g) (Fig. 3f). The Si-2@CP-2@rGO electrode was also evaluated at 0–1.0 V (Figs. S16 and S17 in Supporting information).

The pseudocapacitance behavior of the obtain electrodes was confirmed in the range of 0.01-3.0 V. The CV behaviors of the electrodes were not significantly altered with the scan rate (Figs. S18–S20 in Supporting information and Fig. 4a). The fitting results confirmed that the lithium storage mechanism of the Si, Si-2@CP-2, and Si-2@CP-2@rGO electrodes was controlled by both diffusive and capacitive behaviors (Fig. 4b). The pseudocapacitance ratio of Si, Si-2@CP-2, and Si-2@CP-2@rGO electrodes accounted for up to 72.90%, 89.87%, and 92.23% at 1.0 mV/s (Figs. 4c and d).

Electrochemical impedance is a crucial tool for determining the electrochemical kinetic behavior of electrode materials. The equivalent circuit was shown in Fig. 4e and Fig. S21 (Supporting information). For the Si, Si-2@CP-2, and Si-2@CP-2@rGO electrodes, the R_e was 1.79, 1.74, and 1.30 Ω. While the R_{ct} values were 76.0, 49.6, and 11.8 Ω, respectively (Table S2 in Supporting information). The Si-2@CP-2@rGO electrode featured optimal ion diffusion behavior. In addition, the ion diffusion behaviors were also determined using the galvanostatic intermittent titration technique (GITT) (supporting information). Fig. 4f illustrated that the D_{Li^+} of Si-2@CP-2rGO was superior to that of the Si and Si-2@CP-2 electrodes at various charging and discharging stages. This superiority can be attributed the design of free-standing electrodes, multi-dimensional conductive structure and large specific surface.

To evaluate the utilization of the ultimate electrodes, the Si-2@CP-2@rGO free-standing film and $LiFePO_4$ (LFP) were employed as the negative and positive electrodes to assemble a 2016-type full cell, which achieved a reversible specific capacity of 249.0 mAh/g after 200 cycles at a current density of 0.2 A/g (Fig. 4g and Fig. S22 in Supporting information). Fig. 4h depicted the cycling mechanism of the Si-2@CP-2@rGO//LFP full cell.

The above results confirmed that the Si-2@CP-2@rGO electrode delivered the optimal electrochemical performance. The reasons for this were as follows. (1) The CP and rGO collaborated to create a multi-dimensional conductive structure that facilitated the efficient flow of electrons within the electrode material. (2) The multi-layer buffer and pores structure significantly maintained the reliability of the electrode structure during the cycling process, leading to excellent electrochemical performance. (3) The ultrafine Co particles could reduce the internal resistance of the electrodes and facilitate the electrochemical reactions. The Si-2@CP-2@rGO electrodes had superior properties compared to previously reported Si-based materials (Fig. 4i) [28-35], as vividly demonstrated in Fig. 4j.

SEM analysis was essential for investigating the structural stability of the electrodes. The Si particles with good dispersion were observed in the Si electrode after 10 cycles (Fig. S23a in Supporting information). However, severe agglomerations and cracks appeared on the electrode after 50 cycles, which were attributed to the huge volume change of Si particles (Fig. S23b in Supporting information). The fiber-like structure of the Si-2@CP-2 appeared

slightly adherent after 50 cycles (Figs. S23c and d in Supporting information). However, the Si-2@CP-2@rGO electrode presented a stable electrode structure after 10 and 50 cycles. It was also clearly notice that the rGO nanosheets were well encapsulated (Figs. S23e and f in Supporting information). We confirmed the volume change rates of Si, Si-2@CP-2, and Si-2@CP-2@rGO electrodes were 247.99%, 11.11%, and 5.56%, respectively (Fig. S24 in Supporting information).

The composition of the SEI film was analyzed by XPS. Li_2CO_3 was an inorganic substance of the SEI film, which was harmful to the stabilization of the SEI film [36]. Compared to the Si-2@CP-2 electrode, the peaks of Li_2CO_3 in the Si-2@CP-2@rGO electrode were extremely weak. This indicates that there was no repetitive rupture and regeneration of the SEI film during cycling (Figs. S25a and b in Supporting information) [36]. In addition, the peaks of LiF substance and P-O bond were relatively highlighted, which contributed to maintaining the stability of the electrode structure (Figs. S25c-e in Supporting information) [36]. It was obvious that the Si 2p characteristic peaks in the cycled Si-2@CP-2@rGO electrode were more pronounced, which proved that the SEI film was thin enough to block the signals from the Si substance (Fig. S25f in Supporting information). Both SEM and XPS analyses confirmed that the Si-2@CP-2@rGO electrode could withstand the volume change during cycling.

In summary, the core@multi-shell Si-2@CP-2@rGO film was obtained using a simple electrostatic spinning and electrostatic self-assembly method. The construction of multi-dimensional conductive pathways could enhance the conductivity of the electrodes, while multi-layer buffer structures could effectively reduce the volume change issue of the electrodes. Furthermore, by rationally regulating the reserved pores and introducing ultrafine Co particles, the stability of the electrode structure was further enhanced. The Si-2@CP-2@rGO electrode delivered a high specific capacity of 1221.2 mAh/g after 100 cycles at 0.1 A/g with ICE of 85.1% and 833.3 mAh/g after 200 cycles at 1.0 A/g. Moreover, the assembled Si-2@CP-2@rGO//LFP full cell maintained a specific capacity of 249.0 mAh/g after 200 cycles at 0.2 A/g, highlighting the practical potential of the free-standing Si-2@CP-2@rGO electrode. This work offers new pathways for the thoughtful design of hybrid materials and broadens the applications of flexible electrical devices.

Declaration of competing interest

The authors declare that they have no known competing financial interests or personal relationships that could have appeared to influence the work reported in this paper.

CRediT authorship contribution statement

Xianping Du: Writing – review & editing, Writing – original draft, Methodology, Investigation, Data curation, Conceptualization. **Ying Huang:** Conceptualization. **Chen Chen:** Investigation. **Zhenhe Feng:** Investigation. **Meng Zong:** Investigation.

Acknowledgment

We acknowledge financial support from Natural Science Basic Research Program of Shaanxi Province (No. 2024JC-YBQN-0442). We would also like to acknowledge Analytical & Testing Center of Northwestern Polytechnical University for the equipment support provided for FETEM (FEI Talos F200X) and SEM (FEI Verios G4).

Supplementary materials

Supplementary material associated with this article can be found, in the online version, at doi:10.1016/j.cclet.2024.109990.

References

[1] D. Zhang, L. Li, W. Zhang, et al., Chin. Chem. Lett. 34 (2023) 107122.
[2] H. Li, Z. Chen, Z. Kang, W. Liu, Y. Chen, Energy Stor. Mater. 56 (2023) 40–49.
[3] Q. Chen, L. Huang, J. Liu, Y. Luo, Y. Chen, Carbon 189 (2022) 293–304.
[4] J. Liu, H. Shi, K. Yu, et al., Chin. Chem. Lett. 34 (2023) 108274.
[5] X. Han, L. Gu, Z. Sun, et al., Energy Environ. Sci. 16 (2023) 5395–5408.
[6] M.C. Liu, H.J. Chen, G. Wu, X.L. Wang, Y.Z. Wang, Chin. Chem. Lett. 34 (2023) 107546.
[7] H. Cheng, Y. Liu, Z. Cheng, et al., Chin. Chem. Lett. 35 (2024) 108923.
[8] L. Gu, J. Han, M. Chen, et al., Energy Stor. Mater. 52 (2022) 547–561.
[9] Z.W. Li, M.S. Han, J. Yu, Rare Metals 42 (2023) 3692–3704.
[10] Z. Li, M. Han, P. Yu, J. Lin, J. Yu, Nanomicro Lett. 16 (2024) 98.
[11] T. Bai, W. Wang, G. Xue, et al., ACS Appl. Mater. Interfaces 13 (2021) 57576–57587.
[12] J. Yang, Y. Wang, W. Li, et al., Adv. Mater. 29 (2017) 1700523.
[13] Y. Mu, M. Han, B. Wu, et al., Adv. Sci. 9 (2022) e2104685.
[14] Z. Cui, S.A. He, J. Zhu, et al., Small Methods 6 (2022) e2101484.
[15] M. Shu, X. Li, L. Duan, M. Zhu, X. Xin, Nanoscale 12 (2020) 8819–8827.
[16] M. Zhu, Y. Shen, L. Chang, et al., Nanoscale 12 (2020) 13442–13449.
[17] Y. Han, H. Fu, G. Chen, et al., Chem. Comm. 60 (2024) 220–223.
[18] J. Tang, R.R. Salunkhe, H. Zhang, et al., Sci. Rep. 6 (2016) 30295.
[19] Z. Yang, C. Wu, S. Li, et al., Adv. Funct. Mater. 32 (2022) 2107897.
[20] B. Gang, F. Zhang, X. Li, et al., J Energy Storage 33 (2021) 102132.
[21] T. Li, J. Yin, D. Sun, et al., Small 18 (2022) e2106592.
[22] J. Yu, D. Cai, J. Si, H. Zhan, Q. Wang, J. Mater. Chem. A 10 (2022) 4100–4109.
[23] M. Ma, H. Wang, L. Xiong, et al., Carbon 186 (2022) 273–281.
[24] J. Xu, Q. Yin, X. Li, et al., Nano Lett. 22 (2022) 3054–3061.
[25] V. Shrivastav, S. Sundriyal, A. Kaur, et al., J. Alloys Compd. 843 (2020) 155992.
[26] J. Wang, Y. Huang, X. Du, S. Zhang, M. Zong, Chem. Eng. J. 464 (2023) 142741.
[27] J. Wang, Y. Huang, S. Zhang, et al., J. Mater. Sci. Technol. 147 (2023) 112–123.
[28] Z. Xiao, N. Xia, L. Song, et al., J. Electron. Mater. 47 (2018) 6311–6318.
[29] M.K. Majeed, G. Ma, Y. Cao, et al., Chem. Eur. J. 25 (2019) 11991–11997.
[30] W. An, P. He, Z. Che, et al., ACS Appl. Mater. Interfaces 14 (2022) 10308–10318.
[31] X. Du, Y. Huang, Z. Feng, J. Wang, X. Sun, J. Energy Storage 72 (2023) 108658.
[32] X. Kong, S. Luo, L. Rong, et al., Inorg. Chem. Front. 8 (2021) 4386–4394.
[33] S.F. Liu, C.H. Kuo, C.C. Lin, et al., Electrochim. Acta 403 (2022) 139580.
[34] Z. Ren, S. Liu, J. Chen, et al., Electrochim. Acta 402 (2022) 139556.
[35] P. Fan, T. Mu, S. Lou, et al., Electrochim. Acta 306 (2019) 590–598.
[36] H. Li, H. Li, Z. Yang, et al., J. Colloid Interf. Sci. 627 (2022) 151–159.